PAPER

Check for updates

Disposable paper-based screen-printed electrochemical immunoplatform for dual detection of esophageal cancer biomarkers in patients' serum samples†

Damini Verma,‡[a] Neha Dubey,‡[a] Amit K. Yadav, [ID][a] Anoop Saraya,[c] Rinu Sharma*[b] and Pratima R. Solanki [ID] *[a]

Esophageal cancer is an aggressive disease with an extremely poor prognosis. However, early detection and timely treatment improve the chances of survival. Therefore, in this study, disposable, low-cost, flexible, reagentless, and highly sensitive paper-based screen-printed electrochemical immunosensors were developed for the dual determination of cytokeratin fragment 21-1 (CYFRA-21-1) and tumor protein (TP53) biomarkers in patient serum samples. For this, graphite ink was prepared with the help of a screen-printing machine, a in homepaper-based screen-printed electrode (SPE) substrate was fabricated on its surface. The immobilization of antibodies (CYFRA21-1 and TP53, individually) and BSA were done on inhome paper-based SPE directly using the drop-cast method. The paper-based SPE and other immunoelectrodes were characterized using Fourier transform infrared (FT-IR) spectroscopy, contact angle, scanning electron microscopy (SEM), and energy dispersive X-ray (EDX) spectroscopy. Cyclic voltammetry (CV) and differential pulse voltammetry (DPV) were employed as electrochemical methods for evaluating the performances of immunoplatforms. Under the optimized conditions, the immunoplatforms exhibited a wide linear range for CYFRA21-1 and TP53 from 0.1 to 25 ng mL^{-1} and 0.001–10 ng mL^{-1}, respectively. Comparatively, TP53 showed better results in terms of sensitivity [222.62 µA (log$_{10}$ ng mL^{-1} cm^{-2})$^{-1}$], the limit of quantification (LOQ) [0.018 ng mL^{-1}], and the limit of detection (LOD) [0.005 ng mL^{-1}] in contrast to CYFRA21-1 (sensitivity, 167.07 µA (log$_{10}$ ng mL^{-1} cm^{-2})$^{-1}$; LOQ, 0.041 ng mL^{-1}; and LOD, 0.012 ng mL^{-1}). Thus, the developed immunosensors could potentially be applied as biodevices in clinical laboratories or employed for detecting cancer biomarkers in different human fluids since this method is sensitive, uncomplicated, affordable, portable, and straightforward to develop.

1 Introduction

Esophageal cancer (EC) is the eighth most common cancer worldwide, accounting for around 482 300 new cancer cases with 406,800 registered deaths in 2008.[1] It is a typical upper digestive tract malignant tumor and is a highly aggressive malignancy with a fatality rate that is equivalent to the

[a] *Nano-Bio Laboratory, Special Centre for Nanoscience, Jawaharlal Nehru University, New Delhi, India. E-mail: partima@mail.jnu.ac.in; Tel: 011-26704740/26704699*

[b] *University School of Biotechnology, Guru Gobind Singh Indraprastha University, New Delhi, India. E-mail: rinusharma@gmail.com*

[c] *Department of Gastroenterology, All India Institute of Medical Sciences, Ansari Nagar, New Delhi, India*

incidence rate, owing to its rapid development, delayed diagnosis, as well as poor survival prognosis.[2,3] As per the global cancer statistics in 2018, the total fatality rate of EC ranked sixth, while the incidence rate ranked seventh worldwide.[4] Two primary histological types categorize EC: esophageal squamous cell carcinoma (ESCC) and esophageal adenocarcinoma (EAC). China has the greatest ESCC incidence, which crosses 50% of the global incidence rate.[5] However, with a five-year survival rate (up to 90%), the initial diagnosis could considerably increase the overall survival of individuals.[6] Further, most patients with early EC are typically asymptomatic and show no signs or symptoms of the disease. Therefore, the need arises to detect EC at the earliest stage with the best possible solution.

Cancer biomarkers (CB), also known as biological markers, exhibit outstanding genetic traits typical of malignant cells. CB may be employed as critical elements in the diagnosis, prognosis, or general monitoring of a patient's malignancy state.

Recently, the determination of biomarkers in serum has played a crucial role in recognizing specific cancers and tracking metastasis or recurrence.[7] Operationally, serological tumor markers could be regarded as those molecules whose concentrations can be employed for clinical treatment, prognosis, or diagnosis of malignant disorders.[8] These serological biomarkers, crucial for early recognition of ESCC, have the benefits of high patient acceptance, safety, timely detection, and easy accessibility. Though numerous biochemical markers have been explored for the identification and ongoing monitoring of EC patients, there remains a great need to potentially diagnose serum biomarkers in esophageal cancer through a much simpler technique.

Serum cytokeratin fragment 21-1 (CYFRA21-1) is an established high-potential and well-known biomarker in various cancerous epithelial cells. It is a soluble part of Cytokeratin 19, which is released in the middle stage of apoptosis,[9,10] and is intensely expressed in the serum of >50% of patients having non-small cell lung cancer (NSCLC).[11,12] Tumor protein 53 (TP53) is another promising and emerging cancer biomarker that accounts for uncontrolled cell growth in the body; thus, there is potential for multiple cancer diagnoses.[13] It is a gene that acts as a tumor suppressor biomarker, thus playing a vital part in controlling cell proliferation, genetic stability, and regulating cell growth.[14] When a gene mutation occurs in >50% of all cancers owing to its transformed spatial conformation,[15] such as liver cancer,[16] breast cancer,[17] esophageal cancer,[18] and lung cancer, the ability of TP53 to regulate cells is lost. Consequently, the detection of these protein cancerous biomarkers in various matrices could be used to monitor different human cancers.[19] Therefore, there is a high demand for the development of simple, effective, and economically feasible techniques for determining CB.

Early EC detection is done using an invasive technique; for example, a tissue biopsy of the afflicted area is performed, and its additional evaluation is carried out via non-invasive medical imaging technologies. The standard approaches of endoscopic ultrasonography or computed tomography (CT), positron emission tomography (PET), or magnetic resonance imaging (MRI) scans have restricted efficacy in detection in the early stage as these tests are expensive, inconvenient, unpleasant, and frequently invasive.[20,21] In addition, the optimal treatment strategy for advanced EC is still poorly established. Therefore, a convenient, non-invasive, low-cost technique to diagnose EC on a daily basis is necessary. This has spurred significant attempts to provide quicker, easier approaches that are appropriate for point-of-care (POC) analysis. In comparison to conventional methods for the detection of CB, electrochemical biosensors are preferred due to their relatively high sensitivity, enhanced specificity, the possibility of miniaturization, ease of operation, rapid response, moderate cost, non-invasive detection methods for biomolecules, and being readily quantifiable.[22–25] Many researchers have used different bioreceptors for fabricating biosensors, like aptamers, antibodies,[26,27] proteins, mircoRNA,[28,29] etc., for cancer determination. Among the numerous categories of biosensors, the immunosensor has fascinated researchers and has gotten a lot of attention in the sensing area. Significantly, the electrochemical immunosensors developed utilizing disposable devices like screen-printed electrodes (SPE) have emerged as portable and compact instruments.[30]

Currently, SPE has emerged as a portable biosensing technology for POC and on-site detection.[31] They have demonstrated ductility, can be moulded into several shapes and materials, and are suitable for modification with a wide range of biological components, including antibodies, synthetic recognition elements, enzymes, DNA, and more. In contrast to various substrates, paper-based SPE has attracted immense attention owing to the fascinating characteristics of paper, such as its printability, high availability, biodegradability, ease of manufacture, and affordability. Screen printing technology is the most popular method for developing miniaturized electrochemical cells for paper-based electrochemical devices with the ability to mass produce the sensors at an incredibly cheap cost.[32] SPE comprises three electrode configurations with the reference, auxiliary, and working electrodes printed on the same substrate, i.e., paper. The low dimensions of the SPE allow the demand for only a few microliters for the sample analysis, thereby decreasing the large reagent requirement for the measurement.[33,34] Paper is the most versatile material for measurements because of its availability, affordability, and

Table 1 A comparison of the electrochemical parameters of BSA/anti-TP53/SPE and BSA/anti-CYFRA21-1/SPE immunoplatforms with other electrochemical immunosensors reported in the literature for the detection of TP53 and CYFRA21-1 cancer biomarkers, respectively

Electrode	Technique	Sensitivity	Linear range (ng mL^{-1})	LOD (ng mL^{-1})	Ref.
TP53					
SPCE-CNT/GNP	DPV	—	0.02–10	0.014	30
SPCE-AuNp	LSW	—	2–50	0.05	39
SPCE/magnetic micro-carriers	Amperometry	—	5–150	1.2	40
SPCE/PEI/NPs-Ab B	DPV	—	0.001–10	0.005	41
BSA/anti-TP53/SPE	CV	222.62 µA (log$_{10}$ ng mL^{-1} cm^{-2})$^{-1}$	0.001–10	0.005	This work
	DPV	2.46 µA (log$_{10}$ ng mL^{-1} cm^{-2})$^{-1}$	0.001–10	0.012	
CYFRA21-1					
APTES/nHfO$_2$/ITO saliva	CV	9.28 µA mL ng^{-1} cm^{-2}	2–18	0.21	42
APTES/ZrO$_2$/ITO	CV	2.2 mA mL ng^{-1}	2–16	0.08	43
APTES/ZrO$_2$ RGO/ITO	DPV	0.756 µA mL ng$^{(-1)}$	2–22	0.122	44
Cys-La(OH)$_3$/ITO	DPV	12.044 µA (ng per mL cm^{-2})$^{-1}$	0.001–10.2	0.001	45
BSA/anti-CYFRA21-1/SPE	CV	167.07 µA (log$_{10}$ ng mL^{-1} cm^{-2})$^{-1}$	0.1 to 25	0.012	This work
	DPV	1.56 µA (log$_{10}$ ng mL^{-1} cm^{-2})$^{-1}$	0.1-30	0.17	

simple waste management (*e.g.*, incineration after the sensor is used).[35] Carbon inks are incredibly fascinating for sensing measurements as they are relatively affordable. Also, the carbon-based printed electrode is measured using wide potential windows and low background currents. Further, carbon black acts as a nano-modifier for electrochemical sensors, which is effective in improving the signal-to-noise ratio and reducing the applied voltage for the detection of analyte target, owing to its onion-like structure, the high number of defect sites, large specific surface area, high electric conductivity, as compared to other substrates.[36–38]

Several studies on measuring TP53[30,39–41] and CYFRA21-1 CB by some research groups[42–45] in serum samples using biosensing methods to diagnose cancer are described in Table 1.

Although some of these immunosensors have shown satisfactory results, their measurements have been carried out using large quantities of solution with a traditional three-electrode cell. Also, experiments with non-disposable electrodes like indium tin oxide (ITO) in the case of CYFRA21-1 detection need additional regeneration or polishing steps that are unsuitable for POC detection. At the same time, it is preferable to utilize single disposable sensors to prevent the contamination of samples. Therefore, the need arises to fabricate a biosensor that includes the possibility of using low volumes of reagents and samples, simplicity, and low cost, requiring even < 50 μL of solution for the electrochemical measurements.

Keeping these facts in mind, in the present study, we aimed to fabricate a minimally invasive method for paper-based screen-printed electrochemical immunoplatforms for the early-stage diagnosis of EC biomarkers, *i.e.*, CYFRA21-1 and TP53. For this, graphite ink was made and utilized to fabricate SPE on paper using a screen-printing machine. The sensing region was decorated with antibodies of CYFRA21-1 and TP53 to efficiently capture CYFRA21-1 and TP53 antigens. BSA immobilization on the two immunoplatforms was done to block the graphite ink's free functional groups on the sensing surface area. The SPE and other bioelectrodes were characterized utilizing various analytical techniques like contact angle, energy dispersive X-ray spectroscopy (EDS), scanning electron microscopy (SEM), and Fourier transform infrared spectroscopy (FTIR). Under optimized conditions, cyclic voltammetry (CV) and differential pulse voltammetry (DPV) were utilized to selectively and sensitively monitor EC biomarkers on the working electrode. Finally, the quantitative use of engineered immunoplatforms was applied to measure CYFRA21-1 and TP53 antigens in serum samples from patients.

2 Experimental section

2.1 Chemicals and reagents

The details of chemicals and reagents used in this experiment are given in the (ESI†) file.

2.2 Characterizations

The details of the instruments used for various characterizations are provided in the ESI† file.

2.3 Preparation of graphite-based conductive ink

Graphite-based conductive ink comprises three fundamental elements: a carrier, a binder, and a functional material. In the present study, the deionized water (DI), gum arabic, and graphite powder acted as carriers, binders, and functional materials, respectively. The role of the functional material is to promote conductivity and carrier molecules are involved in homogeneous mixture formation with a functional material. In contrast, a binder controls the mixture's viscosity and holds the elements together. Gum arabic, also known as acacia gum, is a natural gum made from the sap of various species of the Acacia tree. It is composed mainly of polysaccharides and long chains of sugar molecules. These polysaccharides contain different functional groups, including amine functional groups.[46] For synthesizing the ink, 5 mL ink was prepared by using graphite powder with 3 g of gum arabic in 20 mL of boiling DI (100 °C) under continuous stirring. After cooling this mixture, 20 g of graphite powder (∼ 44 nm, particle size) in batches of 5 g under continuous agitation of the mixture was added. The obtained graphite ink was black, homogeneous, and viscous.

2.4 Conductivity analysis of graphite ink

Two different experiments were performed to investigate the lab-made graphite ink's resistance and capacity for conducting the electrical current. Firstly, the electrical resistance was examined utilizing an ohmmeter that showed a resistance of 21.3 Ohm. Next, an LED illumination experiment was performed using the conductive SPE substrate to test the flow charge effect or electrical conductivity. For this, the cathodic end of the LED bulb (1.5 V) was linked to the anodic end of the power supply, and the cathodic end of the power supply was attached to one side of the graphite ink pattern. When the anodic leg of the LED bulb is connected to one side of the graphite ink pattern, the electrical circuit is closed, leading to the illumination of the LED bulb as shown in Fig. 1(b), while in Fig. 1(a), no illumination of LED bulb occurs as the circuit is open, *i.e.*, an incomplete circuit when the anodic leg of the LED bulb is not connected to graphite ink pattern.

2.5 Printing methodology

Screen printing was carried out using a rough paper substrate, that is, grey electro-coated, waterproof silicon carbide. The printing was done with the help of polyester mesh, and two different-sized squeegees were placed on the stencil screen along with medium pressure, providing a printing speed of 500 mm s^{-1}. The SPE consists of three electrodes, namely, working, counter, and reference electrodes. The printed electrodes were then dried at 80 °C in an oven for 15 min. The reference electrode was coated with silver chloride (Ag/AgCl) paste to generate a potential difference between the counter and reference electrodes. Also, an insulating layer (plastic paint) was formed adjacent to the three-electrode system to prevent the back-blowing of the buffer, as shown in Fig. 1(c).

2.5 Collection of human serum samples

The patients' blood samples were collected from the Department of Gastroenterology, All India Institute of Medical
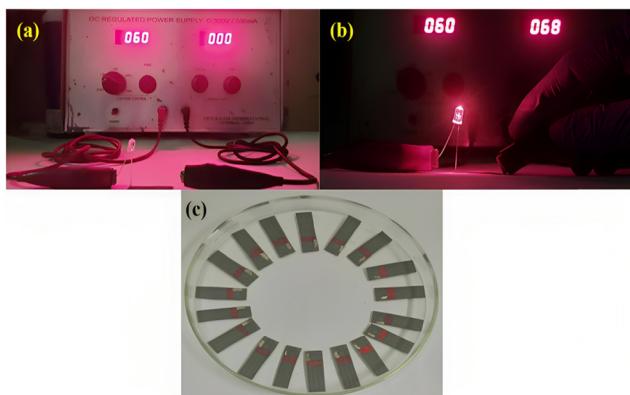
Fig. 1 The LED bulb demonstrates the (a) off-condition in an open circuit, and (b) on-condition in a closed circuit at 59 V of direct current; (c) a three-electrode disposable paper-based SPE.

Sciences (AIIMS), New Delhi. The required ethical permissions were obtained from Guru Gobind Singh Indraprastha University (GGSIPU/IEC/2021-A9) and AIIMS (IEC-106/04.02.2022, RP-03/2022), New Delhi, for collecting the blood samples. To confirm the patients' involvement at the time of blood sample collection, they were asked to fill out the consent form. Before processing, blood samples were collected in a vial and left undisturbed at 4 °C for 20 min. After that, centrifugation of blood samples was done in 5 mL centrifuge tubes for 10 min at 4 °C at 3000 rpm. Finally, the serum was collected from the supernatant, and its aliquots were subsequently made to avoid freeze–thaw cycles. Further, the aliquots were kept at −80 °C for future application.

2.6 The development of paper-based screen-printed immunoplatforms

The immunosensing platform was developed by immobilizing bio-recognition elements (anti-CYFRA 21-1, anti-TP53) on the SPE without any nanomaterial functionalization since the graphite-based conductive ink contains several functional groups that can allow the covalent binding of antibodies due to the presence of gum arabic. The amine functional groups in gum arabic are primarily present in the form of amino acids, which are building blocks of proteins. Gum arabic contains several amino acids, including proline, serine, valine, and alanine, among others. These amino acids have amine functional groups ($-NH_2$) that can participate in various chemical reactions.[46]

For the development of immunoplatforms, the antibodies were directly immobilized on the sensing zone of the paper-based SPE. At first, a mixture was made of 50 μg mL^{-1} of the antibody (anti-CYFRA21-1), 0.4 M EDC (acting as an activator), and 0.1 M NHS (acting as a coupling agent) in a 2 : 1 : 1 ratio in PBS of pH 7.4, with pre-incubation of the mixture at 4 °C for 45 min. This pre-treatment was given so that the carboxylic ($-COOH$) group existing on the anti-CYFRA21-1 Fc fragment forms a covalent bond with the amine functional group present over the working electrode. At first, the anti-CYFRA21-1-

activated carboxyl group led to the formation of the unstable *O*-acylisourea ester that, on further treatment with the NHS, was transformed into a stable intermediate product, *i.e.*, an amine-reactive NHS ester.[47] This activated stable product reacted immediately with the $-NH_2$ groups of the graphite ink present over the working electrode, ensuring the amide bond formation. This was followed by the immobilization of this preincubated mixture solution (15 μL) on the SPE working area and storage of the humid chamber carrying the immobilized anti-CYFRA21-1 SPE at 4 °C for 6 h to fabricate anti-CYFRA21-1/ SPE electrodes, followed by washing with 50 μL PBS (pH 7.4). At the final stage, the immobilization of 2% BSA (5 μL) was done in a humid chamber for 2 h to block the non-specific interaction caused due to unbound functional groups and develop BSA/anti-CYFRA21-1/SPE electrodes. The proposed immunoplatform (BSA/anti-CYFRA21-1/SPE) was prepared for CYFRA21-1 determination and stored in a refrigerator for further utilization.

BSA/anti-TP53/SPE was developed similarly, except for immobilizing anti-TP53 antibodies instead of anti-CYFRA-21-1 antibodies. The illustrations of the fabrication of two screen-printed immunoplatforms, *i.e.*, BSA/anti-CYFRA21-1/SPE and BSA/anti-TP53/SPE for the dual detection of CYFRA21-1 and TP 53, respectively, are depicted in Scheme 1. Further, the detailed functionalization mechanism depicting the surface chemical interactions occurring on the SPE during the fabrication of immunoplatforms is explained and shown in Scheme S1 (ESI†).

3 Results & discussion

3.1 Characterizations

3.1.1 FT-IR analysis. To examine the changes in the functional group region, the FT-IR spectra of bare SPE, anti-CYFRA21-1/SPE, and anti-TP53/SPE are demonstrated in Fig. 2(a)–(c). The bare SPE comprised of graphite powder and gum arabic in Fig. 2(a) showed peaks at 3459 cm^{-1}, 2924 cm^{-1}, and 2853 cm^{-1} that are attributed to O–H stretching (typical of glucosidic bond), and C–H stretching, respectively.[48] Also, other characteristic peaks of graphite at 1649 cm^{-1}, 1456 cm^{-1}, and 1062 cm^{-1} correspond to the COO$^-$ symmetric stretching, C=C aromatic vibrations, and alkoxy C–O stretching vibrations, respectively, while peaks at 846 cm^{-1} and 540 cm^{-1} are attributed typically to the spectrum of gum arabic,[49] which is comprised of amine and hydroxyl groups in its compound structure. In the case of anti-CYFRA21-1/SPE [Fig. 2(b)] and anti-TP53/SPE [Fig. 2(c)] immunoelectrodes, the graphite intensities were decreased. Further, the FTIR spectrum of the anti-CYFRA21-1/SPE electrode shows peaks at 1749 and 1549 cm^{-1} that correspond to the existence of the C–N stretching of the amide bond, signifying the anti-CYFRA-21-1 immobilization at the working area.[50] Similarly, the C–N stretching vibrations due to the amide bond formation are depicted by the anti-TP53/SPE immunoelectrodes at peaks corresponding to the 1648 and 1540 cm^{-1}, respectively, in Fig. 2(c).
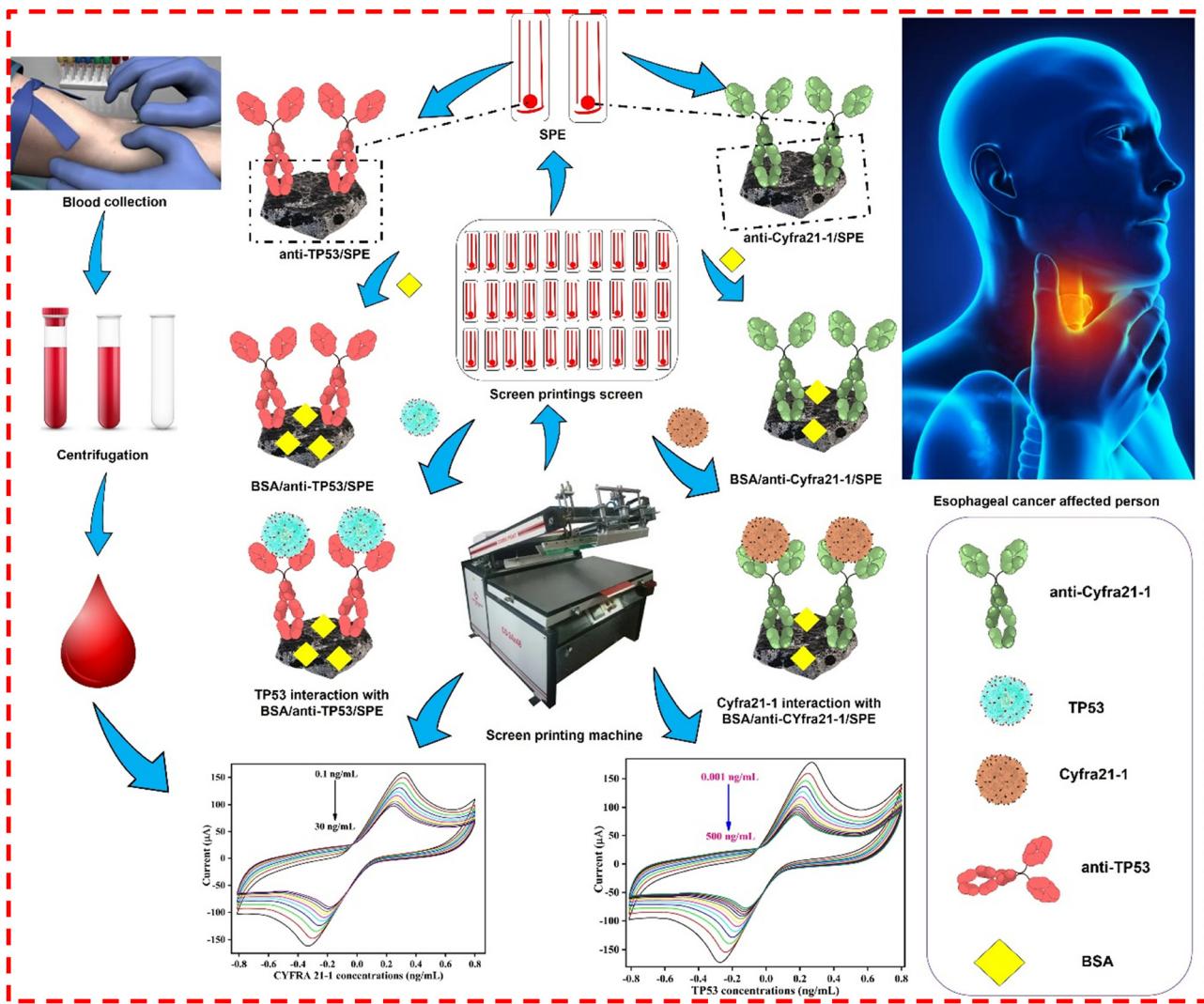
Scheme 1 The fabrication of SPE and the development of two immunoplatforms, *i.e.*, BSA/anti-CYFRA21-1/SPE and BSA/anti-TP53/SPE for the dual detection of CYFRA21-1 and TP53 cancer biomarkers, respectively, in the serum samples of esophageal-affected cancer patients.
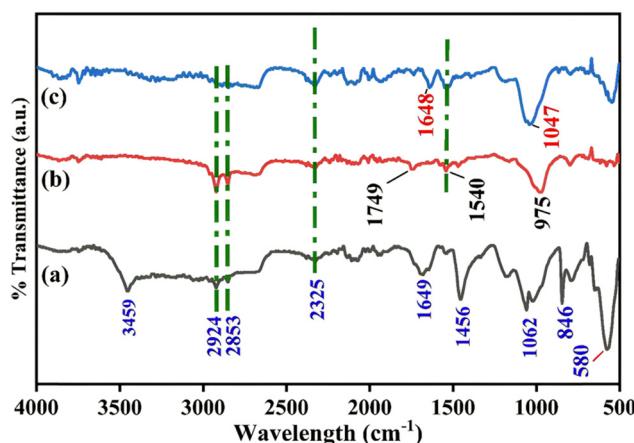
Fig. 2 FTIR analysis of different electrodes: (a) SPE, (b) anti-CYFRA21-1/SPE, and (c) anti-TP53/SPE immunoplatforms.

3.1.2 SEM-EDX analysis. The surface morphology of bare SPE and other immunoplatforms (anti-CYFRA21-1/SPE and anti-TP53/SPE) were studied by SEM. EDS analysis was also used to study the material composition [as shown in Fig. 3]. The scanning electron micrograph [Fig. 3(a) and (b)] shows the extent of particle aggregation or clustering within the graphite ink. The graphite particles depict agglomeration or form clusters due to attractive forces between them. In contrast, the EDX spectrum [Fig. 3(c)] shows the presence of carbon, silicate, sodium, and oxygen, verifying that the ink comprised a conductive carbon source. The presence of sodium and silicate indicated the presence of these elements in the electro-coated waterproof silicon carbide rough paper, whereas, in the case of anti-CYFRA21-1/SPE [Fig. 3(e) and (f)] and anti-TP53/SPE [Fig. 3(i) and (j)], globular structures were seen due to the immobilization of the respective antibodies on its surface. After the immobilization of the antibodies, there was a change in morphology that depicted the successful attachment of biological materials to the paper-based SPE surface. The EDS graph
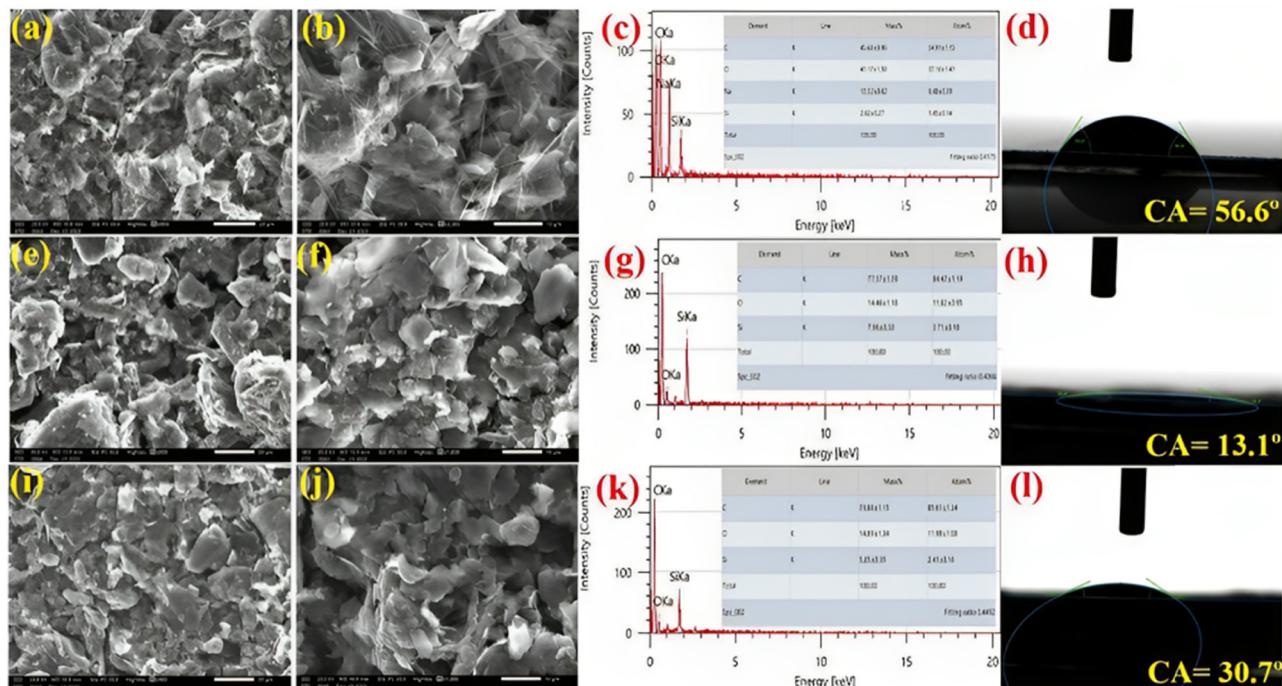
Fig. 3 SEM images of the SPE at (a) low (20 μm) and (b) high (10 μm) magnification; (c) EDS, and (d) CA. SEM images of anti-CYFRA21-1/SPE at (e) low (20 μm) and (f) high (10 μm) magnifications; (g) EDS and (h) CA. SEM images of anti-TP53/SPE at (i) low (20 μm) and (j) high (10 μm) magnifications; (k) EDS and (l) CA.

of anti-CYFRA21-1/SPE [Fig. 3(g)] and BSA/anti-TP53/SPE [Fig. 3(k)] showed the presence of carbon and oxygen, which verified that the graphite ink had increased carbon content in both cases due to the antibody immobilization process.

3.1.3 Contact angle. The sessile drop method was utilized to examine the contact angle (CA) for investigating the hydrophobic or hydrophilic nature of the different developed electrodes after antibody immobilization [Fig. 3]. As depicted in Fig. 3(d), the CA value of the bare paper-based SPE was $\theta = 56.6°$, showing that the electro-coated waterproof, silicon carbide paper is hydrophobic in nature. The hydrophobicity of SPE is necessary for a water-based graphite ink to prevent the ink from peeling off. After that, the CA value of anti-CYFRA21-1/SPE and BSA/anti-TP53/SPE was estimated and it was found that anti-CYFRA21-1/SPE was more hydrophilic ($\theta = 13.1°$) [Fig. 3(h)] than anti-TP53/SPE ($\theta = 30.7°$) [Fig. 3(l)], indicating the greater hydrophilic behavior of anti-CYFRA21-1/SPE than anti-TP53/SPE. A hydrophilic surface fosters the adsorption of biomolecules, such as antibodies or antigens, by creating an environment conducive to their binding. This bioelectrode's hydrophilicity enhances the significant attachment of cancer biomarker antigens (CYFRA21-1 and TP53), thereby leading to an increase in immunosensor sensitivity. Furthermore, hydrophilic surfaces are less likely to interact with non-target proteins or other biomolecules that may be present in the sample, thus minimizing non-specific binding.[51,52]

3.2 Electrochemical studies of BSA/anti-CYFRA21-1/SPE and BSA/anti-TP53/SPE immunoplatforms

3.2.1 pH study. The pH of the electrolyte signifies the influence of the kinetics of redox reactions occurring at the electrode surface. To demonstrate the pH effect of the two proposed immunoelectrodes, BSA/anti-CYFRA21-1/SPE and BSA/anti-TP53/SPE, CV was employed in 50 mM PBS at different pH from the potential window of −0.8 V to +0.8 V at 50 mV s^{-1} consisting of 5 mM $[Fe(CN)_6]^{3-/4-}$. For this experiment, PBS solutions with pH of 6.0, 6.6, 7.0, 7.4, and 8.0 were made carrying the redox species, and each immunoelectrode was analyzed in different pH solutions. It was observed that the two immunoplatforms, i.e., BSA/anti-CYFRA-21-1/SPE [Fig. 4(a)] and BSA/anti-TP53/SPE [Fig. 4(b)], showed the highest anodic peak current in PBS of pH 7.4 as demonstrated in [Fig. 4(a) and (b)]. This may be ascribed to the biological molecules, for example, antibodies, antigens, enzymes, amino acids, and so on, which exist in their natural form, exhibiting enhanced activity at the physiological pH, i.e., 7.4. During the primary or acidic pH, the denaturation of antibodies occurs due to OH$^-$ or H$^+$ ions, while at pH 7.0, redox couples exhibit decreased reactivity, leading to a reduced rate of electron transfer and, consequently, a decrease in the magnitude of the current observed. Moreover, pH adjustments can alter the charge of the electrode surface. At pH 7.0, the electrode acquires a net charge, impacting the electrolyte's attraction or repulsion of charged species. This alteration in the surface charge affects the ability of these species to partake in electrochemical reactions, further contributing to the observed decrease in current.[53,54] Therefore, a PBS buffer of pH 7.4 was selected to carry out further electrochemical experiments.

3.2.2 Electrode study. To conduct an in-depth investigation of the electrochemical activity of the different surface-modified electrodes and the development of two immunosensors before
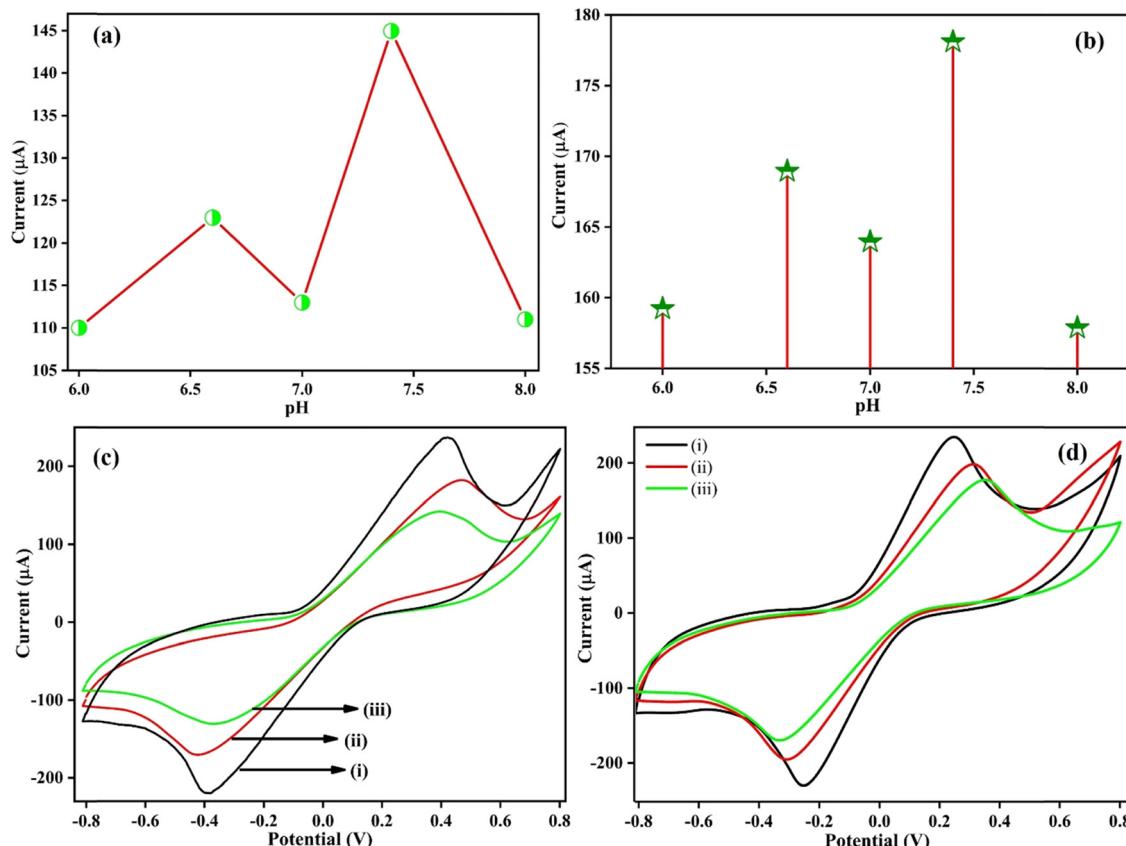
Fig. 4 A pH study of (a) BSA/anti-CYFRA21-1/SPE and (b) BSA/anti-TP53/SPE immunoelectrodes, (c) CV curves of (i) SPE, (ii) anti-CYFRA21-1/SPE, (iii) BSA/anti-CYFRA21-1/SPE and (d) CV curves of (i) SPE, (ii) anti-TP53/SPE (iii) BSA/anti-TP53/SPE immunosensors in PBS.

using them, the electrode study was performed to determine the CYFRA21-1 and TP53 cancer biomarkers. All the electrochemical examinations were conducted using the CV technique from the potential window of -0.8 V to $+0.8$ V in PBS (pH 7.4) consisting of the redox coupler at a scan rate of 50 mV s^{-1} for characterizing the electrode at every functionalization stage and for assessing the binding of antibody-antigen on the surface of the SPE. Fig. 4(c) depicts the comparison of the CV of different modified electrodes, *i.e.*, SPE, anti-CYFRA21-1/SPE, and BSA/anti-CYFRA21-1/SPE, signifying that those variations in the electron transfer kinetics have taken place due to the surface modification step. The SPE showed the maximum current at 236.63 µA due to graphite-based ink since the structure of bulk graphite is composed of sp^2-hybridized graphene layers interacting with weak van der Waals forces and π–π interactions of the delocalized electron orbitals, which enhance the flow of current, *i.e.*, promote electron transfer over the electrode surface.[55,56] However, in the case of the anti-CYFRA-21-1/SPE immunoelectrode, the peak current was reported at 182.22 µA. This decrease in peak current was due to the immobilization of the anti-CYFRA21-1 antibody solution as the insulating nature of the antibody acts as a barrier toward the transportation of electrons from the bulk solution to the electrode surface.[42] The anodic peak current of the BSA/anti-CYFRA-21-1/SPE immunoelectrode (142.15 µA) showed a further

decrease due to the hiding of non-specific active sites by the 2% BSA solution immobilized at the surface of the immunoelectrode, leading to the restricted transfer of electrons from the electrolyte solution to the electrode surface.[57] Moreover, electrochemical impedance spectroscopy (EIS) is a valuable tool for discerning changes in electrode characteristics occurring at the surface. This enables the elucidation of chemical processes and reactions transpiring in that specific region. In line with this, EIS data were acquired for the bare SPE, anti-CYFRA-21-1/SPE, and BSA/anti-CYFRA-21-1/SPE in a PBS solution containing $[Fe(CN)_6]^{3-/4-}$ within a frequency range spanning from 100 kHz to 10 Hz at a potential of 0 V (refer to Fig. S3, ESI†). The Nyquist plot semicircle illustrates each electrode's charge transfer resistance (R_{ct}), a parameter influenced by the dielectric properties of the electrode surface and the electrolyte. This analysis facilitates the characterization of the progressive alterations on the SPE surface during the experimental conditions. The estimated values of various parameters of EIS spectra, such as R_s, R_{ct}, CPE, and Z_w for each electrode, are shown in Table S1 (ESI†).

Fig. 4(d) depicts the electrode study of SPE at 234.77 µA, anti-TP53/SPE (199.43 µA) and BSA/anti-TP53/SPE (177.39 µA) immunoplatforms. The anti-TP53/SPE and BSA/anti-TP53/SPE immunoplatforms also depict a similar trend of anodic peak current, just like in the case of anti-CYFRA21-1/SPE and BSA/

anti-CYFRA21-1/SPE. This suggests that the successful fabrication of the BSA/anti-CYFRA-21-1/SPE and BSA/anti-TP53/SPE immunosensors has occurred.

3.2.3 Scan rate study. The scan rate analyses were performed for different modified electrodes, such as SPE, and two different immunosensors, BSA/anti-CYFRA21-1/SPE and BSA/anti-TP53/SPE, for evaluating the reversibility of the sensor. For this, the CV technique was carried out from 10 to 100 mV s^{-1} in PBS (pH 7.4), having redox species from the potential window of −0.8 V to +0.8 V at 50 mV s^{-1} as depicted in Fig. 5. With the increase in scan rate, there is a rise in the anodic and a decrease in the cathodic peak current as seen in the case of the SPE [Fig. 5(a)], BSA/anti-CYFRA21-1/SPE [Fig. 5(d)] and BSA/anti-TP53/SPE [Fig. 5(g)], respectively.[58] The change in anodic (I_{pa}) as well as cathodic (I_{pc}) peak currents as a function of the square root of scan rate for SPE, BSA/anti-CYFRA21-1/SPE, and BSA/anti-TP53/SPE electrodes are demonstrated in Fig. 5(b), Fig. 5(e), and Fig. 5(h), respectively.[59] The linear fitting graphs of SPE, BSA/anti-CYFRA-21-1/SPE, and BSA/anti-TP53/SPE immunosensors are given by the following eqn (1)–(6):

$$I_{pa(SPE)} = [54.56 \ \mu A \ (s \ mV^{-1}) \ (scan \ rate \ [mV \ s^{-1}])^{1/2}] - 78.02 \ \mu A, \quad R^2 = 0.996 \quad (1)$$

$$I_{pc(SPE)} = -[51.23 \ \mu A \ (s \ mV^{-1}) \ (scan \ rate \ [mV \ s^{-1}])^{1/2}] + 73.10 \ \mu A, \quad R^2 = 0.997 \quad (2)$$

$$I_{pa(BSA/anti-CYFRA21-1/SPE)} = [17.64 \ \mu A \ (s \ mV^{-1}) \ (scan \ rate \ [mV \ s^{-1}])^{1/2}] - 19.55 \ \mu A, \ R^2 = 0.988 \quad (3)$$

$$I_{pc(BSA/anti-CYFRA21-1/SPE)} = -[16.66 \ \mu A \ (s \ mV^{-1}) \ (scan \ rate \ [mV \ s^{-1}])^{1/2}] + 18.25 \ \mu A, \ R^2 = 0.993 \quad (4)$$

$$I_{pa(BSA/anti-TP53/SPE)} = [47.18 \ \mu A \ (s \ mV^{-1}) \ (scan \ rate \ [mV \ s^{-1}])^{1/2}] - 77.73 \ \mu A, \ R^2 = 0.996 \quad (5)$$

$$I_{pc(BSA/anti-TP53/SPE)} = -[43.98 \ \mu A \ (s \ mV^{-1}) \ (scan \ rate \ [mV \ s^{-1}])^{1/2}] + 63.52 \ \mu A, \ R^2 = 0.996 \quad (6)$$

The peak-to-peak distance ($\Delta E_p = E_{pa} - E_{pc}$, where E_{pa} is anodic and E_{pc} is cathodic peak potential) also increases and
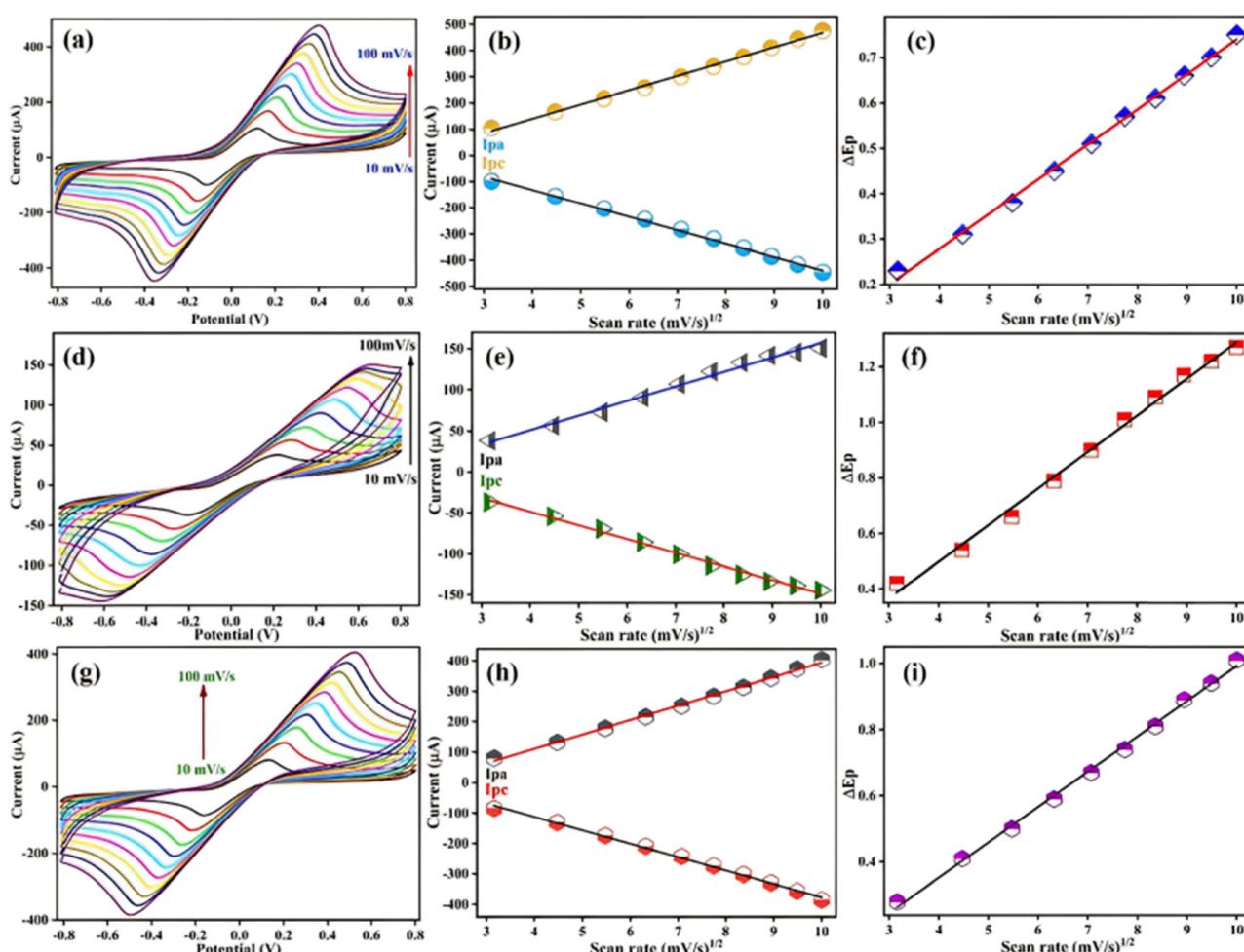
Fig. 5 Scan rate analysis of different electrodes: (a) SPE, (d) BSA/anti-CYFRA21-1/SPE, and (g) BSA/anti-TP53/SPE in PBS. I_{pa} and I_{pc} peak current curves of (b) SPE, (e) BSA CYFRA21-1/SPE and (h) BSA/anti-TP53/SPE electrodes, respectively, with the square root of scan rates. Changes in peak potential (ΔE_p) *versus* the square root of scan rates for (c) SPE, (f) BSA/CYFRA21-1/SPE and (i) BSA/anti-TP53/SPE bioelectrodes, respectively.

moves toward the higher side of potential with the rise in scan rate, resulting in the diffusion-controlled process, *i.e.*, quasi-reversible in nature.[60] Fig. 5(c), Fig. 5(f), and Fig. 5(i), respectively, depict the calibration plots of the shift in the potential peak and the square root of the scan rate obtained for the SPE, BSA/anti-CYFRA21-1/SPE and BSA/anti-TP53/SPE immunoplatforms, respectively. The linear fitting graphs of SPE, BSA/anti-CYFRA-21-1/SPE, and BSA/anti-TP53/SPE immunoplatforms are given in eqn (7) and (8), and (9), respectively:

$$\Delta E_{P_{(SPE)}} = [0.07 \text{ V}(\text{s mV}^{-1}) \text{ (scan rate } [\text{mV s}^{-1}])^{1/2}] - 0.02 \text{ V}, R^2 = 0.997 \quad (7)$$

$$\Delta E_{P_{(BSA/anti-CYFRA21-1/SPE)}} = [0.131 \text{ V}(\text{s mV}^{-1}) \text{ (scan rate } [\text{mV s}^{-1}])^{1/2}] - 0.029 \text{ V}, R^2 = 0.994 \quad (8)$$

$$\Delta E_{P_{(BSA/anti-TP53/SPE)}} = [0.106 \text{ V}(\text{s mV}^{-1}) \text{ (scan rate } [\text{mV s}^{-1}])^{1/2}] - 0.073 \text{ V}, R^2 = 0.997 \quad (9)$$

The Randles–Sevcik formula[61,62] was utilized for estimating the diffusivity or the coefficient of diffusion (D) for the redox coupler, *i.e.*, $[Fe(CN)_6]^{3-/4-}$ as described in eqn (10).[61]

$$I_p = (2.69 \times 10^5)n^{3/2}AD^{1/2}Cv^{1/2} \quad (10)$$

v depicts the scan rate (0.05 V s^{-1}), C depicts the redox coupler concentration (5×10^{-3} mM), D signifies the coefficient of diffusion, A depicts the electrode surface area (0.017 cm^2), n signifies the no. of electrons transferred (*i.e.*, 1), and I_p is the immunoelectrode peak current [*i.e.*, SPE (300.75×10^{-6} A), BSA/antiCYFRA21-1/SPE (106.96×10^{-6} A) and BSA/anti-TP53/SPE (250.76×10^{-6} A)]. From this formula, the diffusion coefficient value was estimated for SPE, BSA/anti-CYFRA21-1/SPE, and BSA/anti-TP53/SPE to be 7.83×10^{-11} cm^2 s^{-1}, 9.90×10^{-12} cm^2 s^{-1} and 5.44×10^{-11} cm^2 s^{-1}, respectively. Among the bio-electrodes, BSA/anti-TP53/SPE represented the high D-value in comparison to BSA/anti-CYFRA-21-1/SPE, showing the improved transfer of electrons at the interface of the electrolyte/electrode of the former electrode, suggesting the remarkable analytical performance of BSA/anti-TP53/SPE immunosensor.

The Brown-Anson model formula[63] was employed for calculating the surface concentrations of SPE, BSA/anti-CYFRA21-1/SPE, and BSA/anti-TP53/SPE immunoplatforms as provided in eqn (11):

$$I_p = n^2F^2\gamma^*Av(4RT)^{-1} \quad (11)$$

T is room temperature, *i.e.*, 300 K, R depicts the gas constant (8.314 J mol^{-1} K^{-1}), F signifies the Faraday constant, *i.e.*, 96485 C mol^{-1}, γ^* represents the absorbed electro-active species' surface concentration, v is the scan rate (0.05 V s^{-1}), A is the electrode surface area and I_p represents the anodic peak current. The surface concentrations of SPE, BSA/anti-CYFRA21-

1/SPE, and BSA/anti-TP53/SPE immunoplatforms are estimated to be 5.70×10^{-5} mol cm^{-2}, 2.02×10^{-4} mol cm^{-2}, and 4.75×10^{-4} mol cm^{-2}, respectively.

Moreover, for estimating the electroactive surface area (A_e)[64] value of the SPE, BSA/anti-CYFRA21-1/SPE, and BSA/anti-TP53/SPE immunoplatforms, the D-values derived in eqn (10) for the respective electrodes were incorporated into eqn (12) for calculating the A_e:

$$A_e = S/(2.69 \times 10^5)n^3CD^{1/2} \quad (12)$$

where S represents the slope of the calibration curve achieved from the calibration curve between the I_{pa} and square root of the scan rate ($v^{1/2}$) as described for the SPE, BSA/anti-CYFRA21-1/SPE and BSA/anti-TP53/SPE immunoplatforms in eqn (1), (3) and (5), respectively. The A_e values for the SPE, BSA/anti-CYFRA-21-1/SPE and BSA/anti-TP53/SPE bioelectrodes are 4.58×10^4 cm^2, 4.16×10^3 cm^2 and 4.75×10^4 cm^2, respectively. This depicts that the BSA/anti-TP53/SPE bioelectrode has more reactive area per unit volume after biomolecule (*i.e.*, antibody and BSA) attachment. Thus, this bioelectrode is more efficient than the BSA/anti-CYFRA21-1/SPE bioelectrode with a 4.75×10^4 cm^2 A_e value.

The scan rate and heterogeneous electron transfer rate constant, *i.e.*, K_s, are two main contributing aspects that are accountable for electron transfer reversible kinetics. Thus, the Laviron formula[65] was used for estimating the K_s values for the SPE, BSA/anti-CYFRA21-1/SPE, and BSA/anti-TP53/SPE, which were 0.98 s^{-1}, 1.74 s^{-1} and 1.29 s^{-1}, respectively, as calculated by eqn (13).

$$K_s = mnFv/RT \quad (13)$$

m depicts the shift in peak potential (V), hence, the higher K_s value achieved in the case of the BSA/anti-TP53/SPE bioelectrode depicts the rapid transfer of electrons among the electrode surface and electrolytic redox coupler. Table 2 summarizes the estimated values of the different electrochemical parameters of the respective electrodes.

The high values of the BSA/anti-TP53/SPE and BSA/anti-CYFRA21-1/SPE immunoelectrodes' interface kinetic parameters suggest that biomolecules like anti-CYFRA21-1, anti-TP53 and BSA effectively play a role in reducing the transfer of electrons at the electrolyte and immunoelectrode interface.

3.3 Electrochemical performance of the BSA/anti-CYFRA21-1/SPE immunoplatform

3.3.1 Electrochemical response study. For evaluating the electrochemical analytical performance of the BSA/anti-CYFRA21-1/SPE immunosensor, the CV technique was employed to determine the different concentrations of CYFRA21-1 cancer

Table 2 Electrochemical parameters of SPE, BSA/anti-CYFRA21-1/SPE, and BSA/anti-TP53/SPE

Electrode	m (V)	D (cm^2 s^{-1})	γ^* (mol cm^{-2})	K_s (s^{-1})	A_e (cm^2)
SPE	0.51	7.83×10^{-11}	5.70×10^{-5}	0.98	4.58×10^4
BSA/anti-CYFRA21-1/SPE	0.90	9.90×10^{-12}	2.02×10^{-4}	1.74	4.16×10^3
BSA/anti-TP53/SPE	0.67	5.44×10^{-11}	4.75×10^{-4}	1.29	4.75×10^4

biomarkers, as depicted in Fig. 6(a). Differential pulse voltammetry (DPV) techniques were also employed, covering the potential range from −0.4 V to +0.8 V (as illustrated in Fig. S1(a), ESI†). These experiments were conducted in a phosphate-buffered saline (PBS) solution containing redox species. The developed BSA/anti-CYFRA21-1/SPE immunoelectrode, following all the standardized experimental settings, was able to estimate the various CYFRA21-1 antigen concentrations from 0.1 to mL^{-1}, *i.e.*, 0.1, 0.3, 1.0, 2.0, 5.0, 15, 20, 25, and 30 ng mL^{-1}. It was observed that on the addition of low to high CYFRA21-1 concentrations, *i.e.*, from 0.1 to 30 ng mL^{-1}, the anodic peak current declined linearly due to the formation of an immune-complex between the molecules of CYFRA21-1 antigens and anti-CYFRA21-1, which acts as an electrical insulator and prevents the kinetics of electron transfer occurring between the redox species and immunoelectrode, thereby hindering the flow of electrons [Fig. 6(a)], and then becomes saturated after a 30 ng mL^{-1} antigen concentration. This affirms that CYFRA21-1 immobilization over the immunoelectrode surface leads to a decrease in the anodic peak current due to the generation of immune-complex quantities on the surface of the immunoelectrode.

After optimizing the experimental conditions, a remarkable linear range was seen with current variations on increasing the

concentration of the CYFRA21-1 antigen from 0.1 to 25 ng mL^{-1}, as shown in Fig. 6(b) [CV] and Fig. S1(b) (ESI†) [DPV]. Linear curves were plotted for CV and DPV peak currents *versus* standard concentrations of CYFRA21-1 as given by eqn (14) and (15), respectively:

$$I_P = [-18.88\ (\mu A\ ng\ mL^{-1}) \times \text{conc. of CYFRA21-1 (ng mL}^{-1})] + 130.42\ \mu A,\ R^2 = 0.989 \quad (14)$$

$$I_P = [-0.131\ (\mu A\ ng\ mL^{-1}) \times \text{conc. of CYFRA21-1 (ng mL}^{-1})] + 33.9\ \mu A,\ R^2 = 0.984 \quad (15)$$

The linear reduction in peak current was proportional to the rise in the concentration of CYFRA21-1 that resulted in the generation of an immune-complex formed between the anti-CYFRA-21-1 as well as on the biosensing platform, *i.e.*, BSA/anti-CYFRA-21-1/SPE. Thus, the decrement in current may be ascribed to the less electro-active areas at the surface of the electrode for the free transfer of electrons, leading to a rise in the thickness of the insulating film. The developed biosensor nanoplatform, *i.e.*, BSA/anti-CYFRA-21-1/SPE, depicted a sensitivity of 167.07 µA (log$_{10}$ ng mL^{-1} cm^{-2})$^{-1}$ (CV) and 1.56 µA (log$_{10}$ ng mL^{-1} cm^{-2})$^{-1}$ (DPV), calculated using eqn (16):
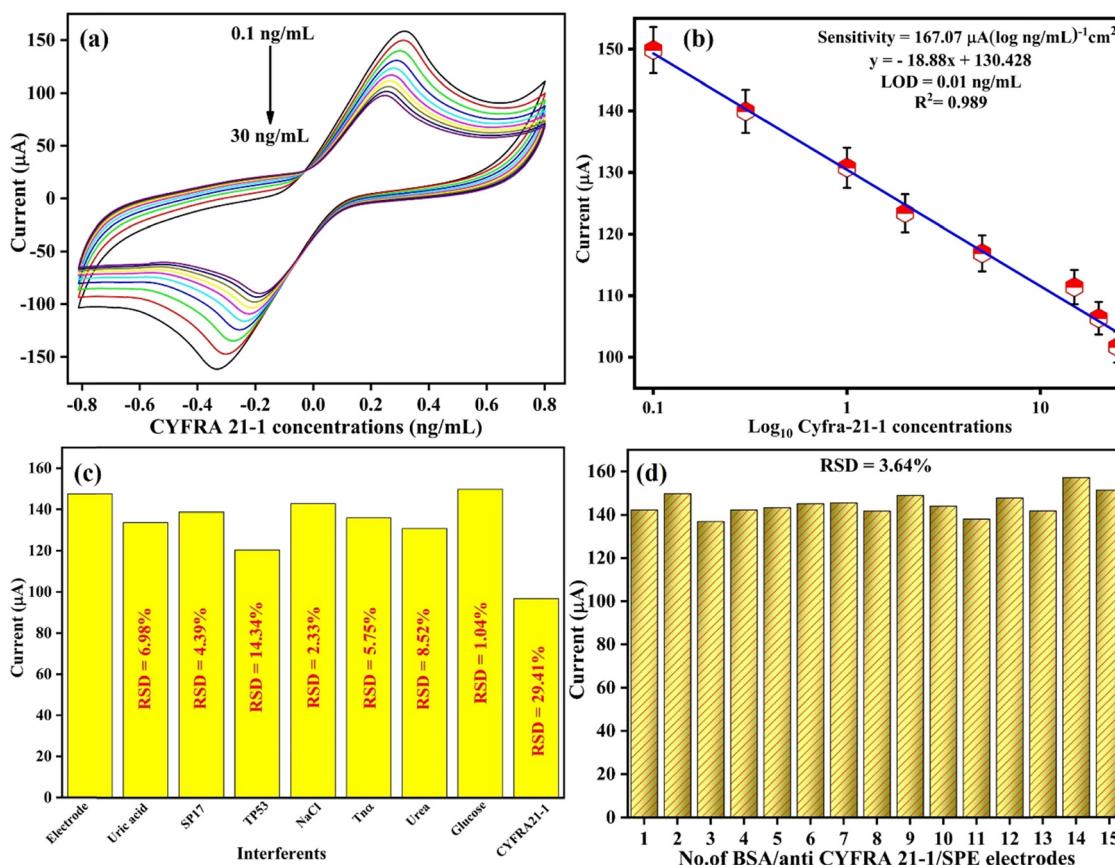
Fig. 6 (a) The sensing analysis of the BSA/anti-CYFRA21-1/SPE immunosensor in PBS against the CYFRA21-1 biomarker. (b) A linear plot for the BSA/anti-CYFRA21-1/SPE immunosensor showing the link between peak currents and the CYFRA21-1 biomarker concentrations. (c) Interferent analysis of the BSA/anti-CYFRA21-1/SPE immunosensor with various interfering agents in PBS containing the redox species. (d) Reproducibility studies of the BSA/anti-CYFRA21-1/SPE immunosensor.

Sensitivity = slope of calibration curve/surface area (0.113 cm²)

$$(16)$$

The limit of detection (LOD) and limit of quantification (LOQ) were found to be 0.012 ng mL^{-1} (eqn (17)) and 0.041 ng mL^{-1} (eqn (18)), respectively.

$$\text{LOD} = 3\sigma/m \qquad (17)$$

$$\text{LOQ} = 10\sigma/m \qquad (18)$$

where the standard deviation of the intercept is depicted by σ and the calibration plot sensitivity is represented by m.

Furthermore, the immunosensor exhibited broad linearity from 0.1 to 25 ng mL^{-1}. The developed immunosensor depicted good outcomes (sensitivity, LOD, and linear range) in comparison with the other previously reported immunosensors on CYFRA21-1 detection, as described in Table 1.

3.3.2 Interferent and reproducibility studies. The significant characteristic of biosensors is selectivity, which depicts the capability of determining a specific analyte and is considered a reliable point for designing a sensor. Hence, the CV technique was utilized for accurately detecting the CYFRA21-1 biomarker, employing several interfering molecules such as analytes found in human serum like NaCl, glucose, uric acid, and urea, and other cancer biomarkers like SP17, TP53, and Tnα that could hinder biosensor functions. Fig. 6(c) depicts the remarkable variation in the intensity of the current on the addition of CYFRA21-1 (30 ng mL^{-1}) alone and shows a slight variation in peak current with other interfering agents, which confirms the selectivity of the developed BSA/anti-CYFRA21-1/SPE immunosensor. Furthermore, the achieved relative standard deviation (%RSD) value of the immunosensor was found to be 1.04% to 29.41%, which is quite good. However, the %RSD for TP53 was reported to be 14.34%, which shows that it is slightly selective towards the TP53 cancer biomarker as compared to the CYFRA21-1 biomarker, which is 29.14%. Since the biosensor demonstrates a selective response to the CYFRA21-1 biomarker and slight interference from other protein mixtures that could affect the signal of CYFRA21-1, it was found that the developed biosensing platform, *i.e.*, BSA/anti-CYFRA21-1/SPE is highly selective for CYFRA21-1 cancer biomarker determination.

Reproducibility is another vital parameter for practical immunosensor utilization. For this, 15 duplicates of BSA/anti-CYFRA21-1/SPE immunoelectrodes were fabricated to investigate the electrode's reproducibility. The CV method was employed to monitor the variations in peak current while
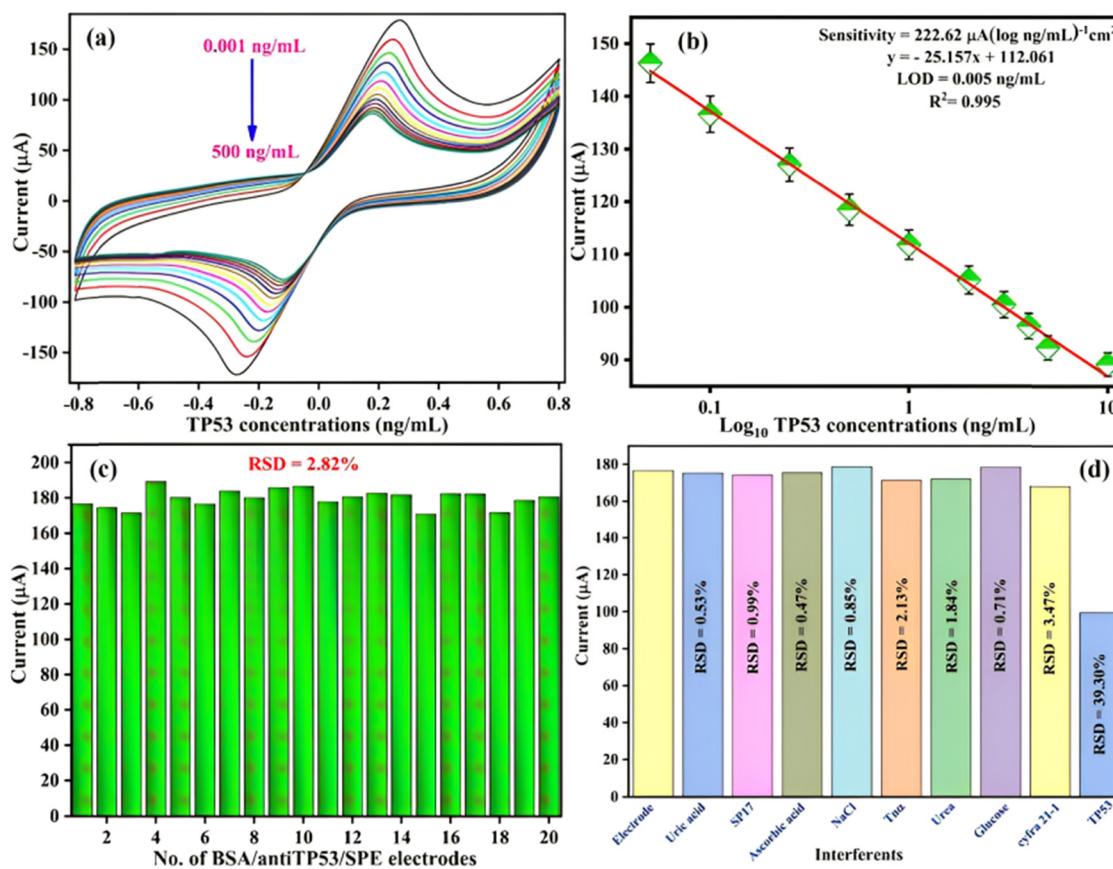
Fig. 7 (a) Electrochemical response analysis of the BSA/anti-TP53/SPE electrode in PBS toward the TP53 biomarker. (b) The calibration plot of the BSA/anti-TP53/SPE electrode depicts the relationship of CV peak currents with different concentrations of the TP53 biomarker. (c) The reproducibility of 20 different BSA/anti-TP53/SPE immunoelectrodes used for the experiment in PBS containing the redox species. (d) Interferent analysis of BSA/anti-TP53/SPE immunoplatforms against various interferents in PBS using the CV technique.

providing similar experimental parameters [Fig. 6(d)]. The bar graph of reproducibility depicted the minimal difference in peak current among the different immunosensors having a %RSD of 3.64%. This value falls under the acceptable limit, showing good accuracy and the capability to promote reproducible results.

3.4 Electrochemical performance of the BSA/anti-TP53/SPE immunoplatform

3.4.1 Electrochemical response study. The sensing or electrochemical response analysis of the BSA/anti-TP53/SPE immunoelectrode was determined as a function of TP53 concentrations from 0.001 to 500 ng mL^{-1}, *i.e.*, 0.001, 0.05, 0.1, 0.25, 0.5, 1.0, 2.0, 3.0, 4.0, 5.0, 10, and 500 ng mL^{-1} and is depicted in Fig. 7(a). The experiments were conducted in PBS buffer (50 mM, 0.9% NaCl) containing redox species (5 mM) at a scan rate of 50 mV s^{-1} in the potential range of −0.8 to +0.8 V using the CV technique. DPV techniques were also employed, covering the potential range from −0.4 V to +0.8 V (as illustrated in Fig. S2(a), ESI†). It was found that the electrochemical peak current gradually decreased linearly with an increased concentration of TP53. We observed that with the addition of a high concentration of TP53, there was a decrease in current that was attributed to the formation of an electrically insulating antigen–antibody complex that perhaps obstructs the electron transfer through [Fe(CN)$_6$]$^{3-/4-}$ redox conversion.[51]

The observed calibration curve between the peak current and antigen concentration obeys eqn (19) (through CV) and eqn (20) (through DPV):

$$I_{pa} = -[25.157\ (\mu A\ ng\ mL^{-1}) \times \text{concentration of TP53 (ng mL}^{-1}) + 112.061\ \mu A],\ R^2 = 0.995 \tag{19}$$

$$I_{pa} = -[0.278\ (\mu A\ ng\ mL^{-1}) \times \text{concentration of TP53 (ng mL}^{-1}) + 15.24\ \mu A],\ R^2 = 0.989. \tag{20}$$

Fig. 7(b) reveals that linearity was obtained in the range of 0.001–10 ng mL^{-1}, with a sensitivity of 222.62 μA (log$_{10}$ ng mL^{-1} cm^{-2})$^{-1}$, LOQ of 0.018 ng mL^{-1}, and LOD of 0.005 ng mL^{-1}. The sensitivity, LOQ, and LOD were estimated as described in eqn (16)–(18). All the parameters were found to be superior to earlier reported immunosensors, as depicted in Table 1. The calibration curve and calculated parameters of BSA/anti-TP53/SPE, done through the DPV technique, are shown in Fig. S2(b) (ESI†).

3.4.2 Interferent and reproducibility studies. Interferant studies were carried out similarly using the BSA/anti-TP53/SPE immunoelectrode to observe the cross-reactivity with other interfering species (described in Section 3.3.2 section) present in human serum. The BSA/anti-TP53/SPE immunoelectrode current response is shown by the bar diagram in Fig. 7(d) in the presence of interferents. The figure shows that negligible variations in current were observed upon adding the interfering species or other biomarkers. In contrast, the decrement in peak current occurred on adding TP53 (5 ng mL^{-1}), which signifies the interaction of the BSA/anti-TP53/SPE immunoelectrode with the added concentration of TP53 and, therefore, the

potential interfering agents were not able to affect the selectivity of the BSA/anti-TP53/SPE immunoelectrode present in the serum. Thus, the fabricated immunoplatforms showed satisfactory %RSD in the range of 0.47% to 39.30% for interfering agents, depicting specificity towards the TP53 antigen.

We also investigated 20 different BSA/anti-TP53/SPE immunoplatforms, fabricated using similar experimental conditions, and measurements were conducted by the CV technique in PBS at the beginning of each experiment as depicted by the bar graph [Fig. 7(c)]. It was observed that the BSA/anti-TP53/SPE immunoplatforms represented a remarkably high reproducibility of 2.82% RSD.

3.5. Clinical sample analysis

3.5.1 Real sample analysis of CYFRA21-1 in patient serum samples. For this experiment, the real samples, *i.e.*, patient serum samples, were used to determine the CYFRA21-1 cancer biomarkers. Here, blood samples were collected from 29 patients at the All-India Institute of Medical Sciences (AIIMS), New Delhi, India, and centrifuged for 10 min at 3000 rpm at 4 °C to obtain the serum from the supernatant, followed by preparation of aliquots to evade the freeze–thaw cycles. For further utilization, serum was kept at −80 °C and analyzed through a conventional method, *i.e.*, ELISA. The measurement of CYFRA21-1 concentrations was performed using a sandwich ELISA kit ELabScience (Catalog No. E-EL-H2077) in triplicate. The manual's instructions were followed, and then an ELISA plate reader was used to measure the absorbance at 450 nm after a colorimetric response was completed. To confirm the outcomes of the developed BSA/anti-CYFRA21-1/SPE immunosensor, CYFRA21-1 concentrations for a series of serum samples were measured using the ELISA technique. The electrochemical response results of the developed immunoelectrode were then assessed using serum samples *via* the CV method. Following that, the same concentration of standard samples was correlated to the current value determined for real patient serum samples. The CV current magnitudes achieved for the concentration of CYFRA21-1 in the real patient sample measured using ELISA and the CYFRA21-1 concentration current in the standard sample were in excellent agreement [Fig. S4, ESI† and Table 3]. Thus, the biosensor could determine the CYFRA21-1 antigen in patient serum samples with a high degree of accuracy in this case since the developed immunosensor showed less than 3% of the %RSD and recovery was in the range of 96.21% to 102.83%.

3.5.2 Real sample analysis of TP53 in patient serum samples. The fabricated BSA/anti-TP53/SPE immunosensor was further used to detect TP53 cancer biomarkers in patient serum samples. For this study, 29 patient serum samples were taken and processed similar to that described in Section 3.5.1. We measured the concentrations of TP53 in triplicate using a sandwich ELISA kit ELabScience (Catalog No. E-EL-H0910). Similar instructions were followed for carrying out the ELISA. The CV method determined the TP53 concentrations in patient serum samples. Further, the ELISA tool was utilized for obtaining the concentrations of the TP53 series for numerous serum

Materials Advances

Table 3 A real sample study utilizing the BSA/anti-CYFRA21-1/SPE electrode with distinct concentrations of CYFRA21-1 cancer biomarker in human serum

Patient samples	CYFRA21-1 concentration determined using ELISA (in ng mL^{-1})	Peak current (μA) obtained with patient serum samples	Peak current (μA) obtained for standard CYFRA21-1	RSD (%)	Recovery (%)
1	2.318	125	123.38	0.92	101.31
2	3.77	138.793	139.92	0.57	99.19
3	7.016	132.781	130.76	1.08	101.54
4	5.421	139.709	139.92	0.11	99.84
5	1.601	116.363	116.88	0.31	99.55
6	2.573	131.408	130.76	0.35	100.49
7	1.273	130.676	130.76	0.05	99.93
8	−0.943	141.052	139.92	0.57	100.80
9	−0.555	137.542	139.92	1.21	98.30
10	13.836	141.052	139.92	0.57	100.80
11	2.956	144.165	139.92	2.73	96.21
12	6.256	141.082	139.92	0.58	100.83
13	1.691	143.035	139.92	1.56	102.22
14	13.836	107.635	106.32	0.87	101.23
15	2.639	112.823	111.38	0.91	101.29
16	4.745	113.189	111.38	1.14	96.84
17	1.24	120.178	123.38	1.86	97.40
18	1.86	129.608	130.76	0.63	99.11
19	0.633	138.122	139.92	0.91	98.71
20	0.713	132.995	130.76	1.2	101.70
21	−0.351	143.89	139.92	1.98	102.83
22	1.034	125.671	123.38	1.3	101.85
23	−0.593	140.96	139.92	0.52	100.74
24	−0.58	139.068	139.92	0.43	99.39
25	−0.713	137.145	139.92	1.42	98.01
26	2.595	130.95	130.76	0.1	100.14
27	−0.797	130	130.76	0.41	99.41
28	−0.898	126.373	123.38	1.69	102.42
29	−0.432	133.88	130.76	1.67	102.38

Table 4 A real sample study utilizing the BSA/anti-TP53/SPE electrode with distinct concentrations of TP53 cancer biomarker in human serum

Patient samples	TP53 conc. determined using ELISA (ng mL^{-1})	Peak current obtained for patient serum samples (μA)	Peak current obtained for standard TP53 samples (μA)	RSD (%)	Recovery (%)
1	261.8	164.45	159.57	2.13	103.06
2	3947	151.9	159.57	3.48	95.19
3	223.7	147.15	146.27	0.42	100.60
4	684.4	160.88	159.57	0.58	100.82
5	363.1	158.08	159.57	0.66	99.07
6	1230	167.96	159.57	3.62	105.26
7	880.6	164.58	159.57	2.19	103.14
8	374.4	147.3	146.27	0.5	100.70
9	690.2	164.09	159.57	1.97	102.83
10	219.6	174.77	159.57	6.43	109.52
11	261.8	156.12	159.57	1.55	97.84
12	523.6	156.06	159.57	1.57	97.80
13	315.8	157.74	159.57	0.82	98.85
14	488	157.77	159.57	0.8	98.87
15	249	150.11	146.27	1.83	102.62
16	221.7	161.43	159.57	0.82	101.16
17	257.5	160.43	159.57	0.38	100.54
18	113.5	157.89	159.57	0.75	98.95
19	408.5	161.86	159.57	1.01	101.43
20	113.9	157.77	159.57	0.8	98.87
21	98.59	159.63	159.57	0.03	100.04
22	275.2	156.95	159.57	1.17	98.36
23	108.8	164.18	159.57	2.01	102.89
24	106.7	159.48	159.57	0.04	99.94
25	199.4	146.6	146.27	0.16	100.22
26	326.8	159.79	159.57	0.1	100.14
27	168.8	173.73	159.57	6.01	108.87
28	67.68	162.41	159.57	1.25	101.78
29	61.29	145.14	146.27	0.55	99.23

samples to authenticate the findings of the developed BSA/anti-TP53/SPE immunosensor as it showed less than 7% of RSD and recovery in the range of 95.19–109.52% (Fig. S3, ESI† and Table 4). These findings showed that the developed BSA/anti-TP53/SPE immunosensing was validated for clinical patient samples. Further, this could be made commercial and portable for accurate and rapid patient screening at early-stage cancer monitoring.

4. Conclusion

In summary, we have developed cost-effective, portable, and disposable electrochemical immunosensor platforms for the dual determination of CYFRA21-1 and TP53 cancer biomarkers. Using the synthesized graphite ink, the three-electrode system was printed and designed with the help of a screen-printing machine on paper. The paper-based substrate was appropriate for the direct immobilization of antigens and antibodies. These SPEs do not require any functionalization for biomolecule immobilization, which makes them different from the other reported immunosensors. The immunoplatforms exhibit excellent characteristics such as high surface functionality, good biocompatibility, and high conductivity. Different characterization methods were used, including FTIR, SEM-EDX, and contact angle, to characterize the other developed electrodes. The electrochemical experiments indicated that the developed BSA/anti-TP53/SPE immunosensing platforms have greater sensitivity towards TP53 cancer biomarkers. The BSA/anti-CYFRA21-1/SPE immunoelectrode showed excellent sensitivity of 167.07 μA $(\log_{10}$ ng mL^{-1} cm$^{-2})^{-1}$, a linear range of 0.1 to 25 ng mL^{-1}, LOQ of 0.041 ng mL^{-1} and LOD of 0.012 ng mL^{-1}, while the BSA/anti-TP53/SPE immunosensor exhibited LOQ of 0.018 ng mL^{-1}, LOD of 0.005 ng mL^{-1}, sensitivity of 222.62 μA $(\log_{10}$ ng mL^{-1} cm$^{-2})^{-1}$ and linear range of 0.001–10 ng mL^{-1}, respectively. The fabricated BSA/anti-TP53/SPE immunoplatforms reported better sensitivity, linear range, LOD, and LOQ results. In addition, the detection outcomes for both the developed immunosensors demonstrated a good correlation with the standard ELISA technique for patient serum samples. Therefore, the developed immunosensing nanoplatforms could be well-accomplished biodevices for medical laboratories. Also, the immunosensing nanoplatforms depicted a remarkable selectivity toward the respective antigens, as shown by the assays employing the complex. Overall, the proposed immunosensing platform describes a high potency for use as a robust technique for the dual determination of CYFRA21-1 and TP53 cancer biomarkers. Thus, the developed disposable paper-based immunosensing platform could be used as a diagnostic tool due to its portable, simple, and affordable nature for the detection of other biomarkers.

Live subject statement

All experimental work was conducted following the Ethical guidelines concerning the human subjects approved by AIIMS and IPU, Delhi. Consent forms were also filled and taken from the patient for this study.

Author contributions

D. V.: methodology, formal analysis, writing – original draft. N. D.: methodology writing – review & editing. A. K. Y.: formal analysis, writing – review & editing. R. S.: conceptualization, supervision. P. R. S.: conceptualization, supervision.

Conflicts of interest

The authors declare that they have no conflict of interest.

Acknowledgements

References

1 A. Jemal, F. Bray, M. M. Center, J. Ferlay, E. Ward and D. Forman, Ca-Cancer J. Clin, 2011, 61, 69–90.

2 K. D. Crew and A. I. Neugut, Seminars in oncology, Elsevier, 2004, vol. 31, pp. 450–464.

3 P. Vaupel and A. Mayer, Cancer Metastasis Rev., 2007, 26, 225–239.

4 F. Bray, J. Ferlay, I. Soerjomataram, R. L. Siegel, L. A. Torre and A. Jemal, Ca-Cancer J. Clin., 2018, 68, 394–424.

5 M. Arnold, I. Soerjomataram, J. Ferlay and D. Forman, Gut, 2015, 64, 381–387.

6 S.-L. Zhou and L.-D. Wang, World J. Gastroenterol., 2010, 16, 2348.

7 M. R. Hasan, M. S. Ahommed, M. Daizy, M. S. Bacchu, M. R. Ali, M. R. Al-Mamun, M. A. S. Aly, M. Z. H. Khan and S. I. Hossain, Biosens. Bioelectron.: X, 2021, 8, 100075.

8 T. L. Moskal, S. Huang, L. M. Ellis, H. A. Fritsche Jr and S. Chakrabarty, Cancer Epidemiol. biomarkers Prev. a Publ. Am. Assoc. Cancer Res. cosponsored by Am. Soc. Prev. Oncol., 1995, vol. 4, pp. 127–131.

9 R. Malhotra, A. B. Urs, A. Chakravarti, S. Kumar, V. K. Gupta and B. Mahajan, Tumor Biol., 2016, 37, 9263–9271.

10 Y.-L. Huang, J. Chen, W. Yan, D. Zang, Q. Qin and A.-M. Deng, Tumor Biol., 2015, 36, 3137–3145.

11 N. Kanaji, S. Bandoh, J. Fujita, T. Ishii, T. Ishida and A. Kubo, *Lung Cancer*, 2007, **55**, 295–302.

12 L. Zhang, D. Liu, L. Li, D. Pu, P. Zhou, Y. Jing, H. Yu, Y. Wang, Y. Zhu and Y. He, *BMC Cancer*, 2017, **17**, 1–14.

13 H. Afsharan, F. Navaeipour, B. Khalilzadeh, H. Tajalli, M. Mollabashi, M. J. Ahar and M.-R. Rashidi, *Biosens. Bioelectron.*, 2016, **80**, 146–153.

14 W. Zhao, H. Li, Y. Tang, M. Liu, S. Wang and R. Yu, *Microchim. Acta*, 2019, **186**, 1–8.

15 N. Bidar, M. Amini, F. Oroojalian, B. Baradaran, S. S. Hosseini, M.-A. Shahbazi, M. Hashemzaei, A. Mokhtarzadeh, M. R. Hamblin and M. de la Guardia, *TrAC, Trends Anal. Chem.*, 2021, **134**, 116143.

16 T. Kato, D. Murata, R. A. Anders, H. Sesaki and M. Iijima, *Biochem. Biophys. Res. Commun.*, 2021, **549**, 83–90.

17 M. K. Rana, A. P. Rana and U. Khera, *Cureus*, 2021, **13**(11), e19395.

18 L. Suzuki, D. Nieboer, J. J. B. van Lanschot, M. C. W. Spaander, L. H. J. Looijenga and K. Biermann, *Biomarkers Med.*, 2020, **14**, 785–793.

19 X. Yin, B. Chen, M. He and B. Hu, *Microchim. Acta*, 2019, **186**, 1–8.

20 P. H. Montero and S. G. Patel, *Surg. Oncol. Clin.*, 2015, **24**, 491–508.

21 C. M. Miyazaki, R. Mishra, D. J. Kinahan, M. Ferreira and J. Ducrée, *Colloids Surf., B*, 2017, **158**, 167–174.

22 S. Mishra, D. Saadat, O. Kwon, Y. Lee, W.-S. Choi, J.-H. Kim and W.-H. Yeo, *Biosens. Bioelectron.*, 2016, **81**, 181–197.

23 X.-J. Chen, X.-Q. Zhang, Q. Liu, J. Zhang and G. Zhou, *J. Nanobiotechnol.*, 2018, **16**, 1–17.

24 J. Chang, X. Wang, J. Wang, H. Li and F. Li, *Anal. Chem.*, 2019, **91**, 3604–3610.

25 X. Zhang, Y. Yu, J. Shen, W. Qi and H. Wang, *Talanta*, 2020, **212**, 120794.

26 A. Kalkal, R. Pradhan, S. Kadian, G. Manik and G. Packirisamy, *ACS Appl. Bio Mater.*, 2020, **3**, 4922–4932.

27 A. Kalkal, A. Tiwari, D. Sharma, M. K. Baghel, P. Kumar, R. Pradhan and G. Packirisamy, *Int. J. Biol. Macromol.*, 2023, 127260.

28 S. S. Low, Y. Pan, D. Ji, Y. Li, Y. Lu, Y. He, Q. Chen and Q. Liu, *Sens. Actuators, B*, 2020, **308**, 127718.

29 C. Pothipor, N. Aroonyadet, S. Bamrungsap, J. Jakmunee and K. Ounnunkad, *Analyst*, 2021, **146**, 2679–2688.

30 M. Giannetto, M. V. Bianchi, M. Mattarozzi and M. Careri, *Anal. Chim. Acta*, 2017, **991**, 133–141.

31 F. T. C. Moreira, S. Sharma, R. A. F. Dutra, J. P. C. Noronha, A. E. G. Cass and M. G. F. Sales, *Biosens. Bioelectron.*, 2013, **45**, 237–244.

32 M. U. Ahmed, M. M. Hossain, M. Safavieh, Y. L. Wong, I. A. Rahman, M. Zourob and E. Tamiya, *Crit. Rev. Biotechnol.*, 2016, **36**, 495–505.

33 J. P. Metters, R. O. Kadara and C. E. Banks, *Analyst*, 2011, **136**, 1067–1076.

34 Z. Taleat, A. Khoshroo and M. Mazloum-Ardakani, *Microchim. Acta*, 2014, **181**, 865–891.

35 A. W. Martinez, S. T. Phillips, G. M. Whitesides and E. Carrilho, *Anal. Chem.*, 2010, **82**(1), 3–10.

36 V. Mazzaracchio, M. R. Tomei, I. Cacciotti, A. Chiodoni, C. Novara, M. Castellino, G. Scordo, A. Amine, D. Moscone and F. Arduini, *Electrochim. Acta*, 2019, **317**, 673–683.

37 P. B. Deroco, R. C. Rocha-Filho and O. Fatibello-Filho, *Talanta*, 2018, **179**, 115–123.

38 M. R. Tomei, F. Arduini, D. Neagu and D. Moscone, *Talanta*, 2018, **189**, 262–267.

39 O. Amor-Gutiérrez, E. Costa-Rama, N. Arce-Varas, C. Martínez-Rodríguez, A. Novelli, M. T. Fernández-Sánchez and A. Costa-García, *Anal. Chim. Acta*, 2020, **1093**, 28–34.

40 M. Pedrero, F. J. Manuel de Villena, C. Muñoz-San Martín, S. Campuzano, M. Garranzo-Asensio, R. Barderas and J. M. Pingarrón, *Biosensors*, 2016, **6**, 56.

41 G. Ibáñez-Redín, N. Joshi, G. F. do Nascimento, D. Wilson, M. E. Melendez, A. L. Carvalho, R. M. Reis, D. Gonçalves and O. N. Oliveira, *Microchim. Acta*, 2020, **187**, 1–10.

42 S. Kumar, S. Kumar, S. Tiwari, S. Augustine, S. Srivastava, B. K. Yadav and B. D. Malhotra, *Sens. Actuators, B*, 2016, **235**, 1–10.

43 S. Kumar, S. Kumar, S. Tiwari, S. Srivastava, M. Srivastava, B. K. Yadav, S. Kumar, T. T. Tran, A. K. Dewan and A. Mulchandani, *Adv. Sci.*, 2015, **2**, 1500048.

44 S. Kumar, J. G. Sharma, S. Maji and B. D. Malhotra, *Biosens. Bioelectron.*, 2016, **78**, 497–504.

45 S. Tiwari, P. K. Gupta, Y. Bagbi, T. Sarkar and P. R. Solanki, *Biosens. Bioelectron.*, 2017, **89**, 1042–1052.

46 N. Prasad, N. Thombare, S. C. Sharma and S. Kumar, *Ind. Crops Prod.*, 2022, **187**, 115304.

47 A. K. Yadav, D. Verma, A. Kumar, A. N. Bhatt and P. R. Solanki, *Int. J. Biol. Macromol.*, 2023, **239**, 124325.

48 C. A. Ibekwe, G. M. Oyatogun, T. A. Esan and K. M. Oluwasegun, *Am. J. Mater. Sci. Eng.*, 2017, **5**, 28–36.

49 M. M. A. Mansour, Y. E. Zidan, A. El Fettouh, A. Abd El Hakim, M. M. Allam, H. M. Ali, M. Akrami and M. Z. M. Salem, *J. Chem.*, 2021, **2021**, 1–21.

50 M. A. Ali, S. Srivastava, P. R. Solanki, V. Reddy, V. V. Agrawal, C. Kim, R. John and B. D. Malhotra, *Sci. Rep.*, 2013, **3**, 2661.

51 A. K. Yadav, P. Gulati, R. Sharma, A. Thakkar and P. R. Solanki, *Talanta*, 2022, **243**, 123376.

52 A. K. Yadav, D. Verma and P. R. Solanki, *ACS Appl. Bio Mater.*, 2023, **6**(10), 4250–4268.

53 N. D. McMillion, A. W. Wilson, M. K. Goetz, M. C. Chang, C. C. Lin, W. J. Feng, C. C. L. McCrory and J. S. Anderson, *Inorg. Chem.*, 2018, **58**, 1391–1397.

54 Y. Kumar, P. Pramanik and D. K. Das, *Heliyon*, 2019, **5**(7), e02031.

55 T. Tran and K. Kinoshita, *J. Electroanal. Chem.*, 1995, **386**, 221–224.

56 D. D. L. CHUNG, *J. Mater. Sci.*, 2002, **37**, 1475–1489.

57 A. K. Yadav, D. Verma, G. B. Lakshmi, S. Eremin and P. R. Solanki, *Food Chem.*, 2021, **363**, 130245.

58 A. K. Yadav, D. Verma and P. R. Solanki, *Mater. Today Chem.*, 2021, **22**, 100567.

59 D. Verma, A. K. Yadav, M. D. Mukherjee and P. R. Solanki, *J. Environ. Chem. Eng.*, 2021, **9**(4), 105504.

60 D. Verma, T. K. Dhiman, M. D. Mukherjee and P. R. Solanki, *J. Electrochem. Soc.*, 2021, **168**(9), 097504.

61 D. Verma, D. Chauhan, M. Das Mukherjee, K. R. Ranjan, A. K. Yadav and P. R. Solanki, *J. Appl. Electrochem.*, 2021, **51**, 447–462.

62 D. Verma, K. R. Ranjan, M. Das Mukherjee and P. R. Solanki, *Biosens. Bioelectron.: X*, 2022, 100217.

63 D. Verma, R. K. Sajwan, G. Lakshmi, A. Kumar and P. R. Solanki, *Environ. Sci.: Nano*, 2022, **9**, 3992–4006.

64 G. Lakshmi, A. K. Yadav, N. Mehlawat, R. Jalandra, P. R. Solanki and A. Kumar, *Sci. Rep.*, 2021, **11**, 1–14.

65 D. Chauhan, A. K. Yadav and P. R. Solanki, *Microchim. Acta*, 2021, **188**, 1–11.